Communications in Physics, Vol. 32, No. 3 (2022), pp. 307-318
DOI: https://doi.org/10.15625/0868-3166/16754

TEMPERATURE-MEDIATED PHASE TRANSFORMATION AND OPTICAL PROPERTIES OF TUNGSTEN OXIDE NANOSTRUCTURES PREPARED BY FACILE HYDROTHERMAL METHOD

PHAM NGOC LINH[1], LUU THI LAN ANH[1], NGUYEN THI TUYET MAI[2], PHAM VAN THANG[1], NGUYEN HUU LAM[1] AND NGUYEN CONG TU[1,†]

[1]*School of Engineering Physics, Hanoi University of Science and Technology, Hanoi, Vietnam*
[2]*School of Chemical Engineering, Hanoi University of Science and Technology, Hanoi, Vietnam*

E-mail: [†]tu.nguyencong@hust.edu.vn

Received 29 November 2021; *Accepted for publication 16 May 2022*; *Published 2 June 2022*

Abstract. *Different tungsten oxide nanocrystals were synthesized via a facile hydrothermal process – one step and free of additives - at different reaction temperatures and in a highly acidic environment. The phase transformation of samples, followed by the change of morphology and optical band gap, was observed as the reaction temperature varied from room temperature (23˚C) to 220˚C. The crystal phase transformed from monoclinic $WO_3 \cdot 2H_2O$ to orthorhombic $WO_3 \cdot H_2O$, then to monoclinic WO_3 when the reaction temperature increased from room temperature to 100˚C, then to 220˚C, respectively. Corresponding to the phase transformation, the optical band gap increased from 2.43 eV to 2.71 eV, and the morphology varied from nanoplate to nanocuboid. The effect of the reaction temperature on the phase transformation was assigned to the dehydration process, which became stronger as the reaction temperature increased. These results gave an insight into the phase transformation and implied a simple method for manipulating the crystal phase and morphology of tungsten oxide nanostructures for various applications.*

Keywords: Tungsten oxide; phase transformation; reaction temperature; optical band gap; facile hydrothermal method.

Classification numbers: 81.16.-c; 81.40.-z; 78.67.-n; 64.70.Nd.

I. INTRODUCTION

Among various metal oxide semiconductors, tungsten oxide (WO_3) is one of the most studied materials due to its high potential for various applications in monitoring and processing environment, harvesting and/or saving energy such as gas sensors [1, 2], electrochromic devices [3], photocatalysis [4, 5], energy-related applications [6, 7], surface-enhanced Raman scattering [8]... Recent developments in designing and controlling WO_3 nanostructure preparation have made these potentials more appealing for researchers and engineers [1–10]. Up to now, tungsten oxide has been prepared by various methods, which can be named as sol-gel [11], physical vapor

deposition [12], pulsed laser deposition [13], solvothermal [14], hydrothermal [9, 15], or electrospinning [16]... Among them, the wet chemical method, especially the hydrothermal method, is the most used because of its advantages such as simple, cost-effective, good crystallized, and homogeneous products, and could meet the requirement for bath products [17].

In the facile hydrothermal treatment – one-step and free of additives, several processing parameters that could be used as controlling parameters such as the acidity [9, 18, 19], reaction time [18,20,21], reaction temperature [18,22–24]. By varying these parameters, researchers could manipulate the crystal structure and morphology of the products, which then affected the potential for applications. For example, Jamali *et al.* [9] studied the effect of the acidity (in moderate range with pH= 1÷2.5), reaction time, and post calcination on WO_3 nanostructures prepared via the facile hydrothermal method. Wang *et al.* [19] tuned the morphology of tungsten oxide by varying the pH of the precursor solutions in hydrothermal treatment but the phase transformation was not observed. Adhikari and co-workers [18] studied the effect of both acidity (using different fluoroboric acid concentrations - 2 M to 5 M), reaction time (0 to 8 hours), reaction temperature (160-200˚C) on the phase transformation and morphology of WO_3 prepared via hydrothermal route, but in this work, they used a complicate washing and drying processes. Zhang *et al.* [22] reported the phase transformation and the change of morphology when they varied the HNO_3 concentration and hydrothermal temperature (but at only two temperatures of 120 and 180˚C). Recently, Liu and co-workers [23] investigated the effect of the hydrothermal temperature (in the range from 120 to 200˚C) and time (12h-32h) on the crystal structure, morphology, and visible-light-driven photocatalysis of WO_3 products, but in their work, no phase transformation was observed due to the post calcination at 600˚C. Tehrani *et al.* [21] studied the effects of reaction time on the morphology and phase transformation of tungsten oxide nanostructure prepared by a facile hydrothermal route but only at 180˚C. Liu and co-workers [23] prepared WO_3 1-D nanorods by hydrothermal method at different temperatures and reaction times, but no phase transformation was reported. In our previous work, we studied the effect of reaction time on the phase transformation of tungsten oxide prepared by a facile hydrothermal route in a highly acidic environment, but only at 180˚C [20]. Based on the above results and a literature survey, there is still a lack of a systematic study about the effect of reaction temperature on the phase transformation of WO_3 prepared via a facile hydrothermal route, especially in a highly acidic environment. The systematic study could give an insight view into the phase transformation, which then benefits the design and controlling prepare the phase junction. It is noteworthy that, recently, phase junction is an effective structure to promote the electron-hole separation for carrier-driven phenomena like photocatalyst or water splitting [25–27].

This work is an effort to systematically study the effect of reaction temperature on the phase transformation of tungsten oxide nanostructures prepared via the hydrothermal route in a highly acidic environment. The reaction temperature was varied in a wide range from room temperature (RT) to 220˚C. The physical properties, i.e., crystal phase, the morphology, characteristic bonding on the surface, and the optical band gap, were examined with X-ray diffraction (XRD), field emission scanning electron microscopy (FESEM), Raman scattering, and diffuse reflectance spectroscopy (DRS) data. The mechanism of the crystallization and the growth process were also discussed to give an insight into the effect of reaction temperature on the phase transformation.

II. EXPERIMENT

II.1. Material preparation

In this work, all chemicals are at reagent grade and were used as received without any further purification. The preparation process of tungsten oxide nanostructures was detailed as follows: dissolving 8.25 g of $Na_2WO_4 \cdot 2H_2O$ (99.5%, Xilong) in 25 ml bi-distilled water to obtain 25 ml of Na_2WO_4 1M solution; adding gradually 45 ml HCl (37 wt.%, Xilong) then 15 ml bi-distilled water into Na_2WO_4 solution under intensely magnetic stirring to get the precursor suspension. The precursor suspension was stirred vigorously for 4 hours, then put into a 100-ml Teflon-lined stainless-steel autoclave to carry out the hydrothermal progress for 12h at different reaction temperatures in the range from RT (23˚C) to 220˚C. The pH value of the precursor solution was - 1.1 measured by pH meter Hanna HI2020-02, which confirmed the highly acidic environment of precursor suspension. After 12h of hydrothermal process, the agglomerate product was collected and cleaned with bi-distilled water several times. The cleaned aggregation was dried in ambient air at 80˚C for 24 h, then ground into powder for further analysis and measurement. The samples were named via reaction temperatures, i.e., RT, T100, T120, T150, T180, T200, and T220 corresponding to the reaction temperatures at RT, 100, 120, 150, 180, 200, and 220˚C, respectively.

II.2. Analysis

The morphology of samples was investigated via analyzing FESEM images measured by field emission scanning electron microscope JEOL JSM-7600F. Analyzing the XRD pattern recorded by X'pert Pro (PANalytical) MPD using Cu-Kα radiation ($\lambda = 1.54065$ Å) was used to examine the crystalline properties of samples. XRD analysis was carried out using HighScore Plus software using the ICDD database. Raman spectroscopy, acquired by the Renishaw Invia Raman Microscope with 633 nm laser light, was used to study characteristic vibrations on samples' surfaces. The DRS measured by the diffuse reflectance spectrometer JASCO V-750 was used to study the optical properties of samples.

III. RESULTS AND DISCUSSION

III.1. FESEM analysis

Figure 1 presents the FESEM images of all samples, which implied a variety of morphology from nanosheet to nanocuboid as the reaction temperature increased. In detail, the sample prepared at RT (sample RT) had nanoplate morphology with sharp edges and a thickness of approximately 10 nm (Fig. 1a), but these nanoplates were notably aggregated together. As the reaction temperature increased to 100 and 120˚C (samples T100 and T120), the nanoplate morphology was also obtained but with a rectangular shape, smooth edges, and well separated (Figs. 1b and 1c). The nanoplates in samples T100 and T120 had an average thickness of about 20 and 26 nm, respectively, which seems to increase with reaction temperature. When the reaction temperature increased to 150˚C (sample T150), besides nanoplate morphology, nanocuboid morphology was also observed (Fig. 1d). The nanocuboid morphology became dominant and completely dominated in samples prepared at higher temperatures (samples T180, T200, and T220 in Figs. 1e, 1f, and 1g, respectively). It is noteworthy that the average dimension of nanocuboid increased when reaction temperature increased from 180˚C ($\sim$ 42 nm) to 200˚C ($\sim$ 53 nm) and then decreased as

reaction temperature increased further to 220˚C (about 43 nm). The variation of morphology from sharp nanoplate to smooth rectangular plate and then to nanocuboid with the increase of reaction temperature implied a simple method to prepare tungsten oxide nanostructure with designed morphology.

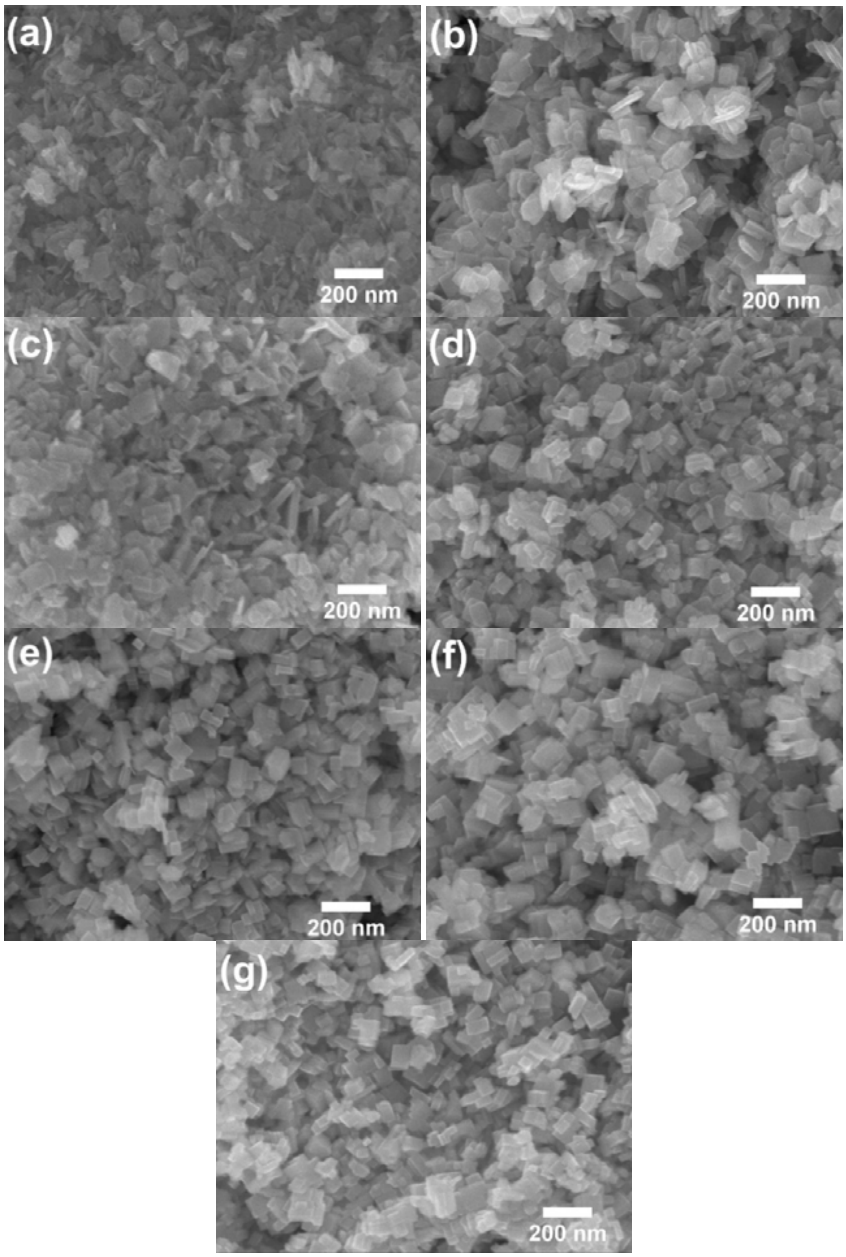

Fig. 1. FESEM images of samples prepared at different reaction temperatures: samples (a) RT, (b) T100, (c) T120, (d) T150, (e) T180, (f) T200 and (g) T220.

III.2. XRD analysis

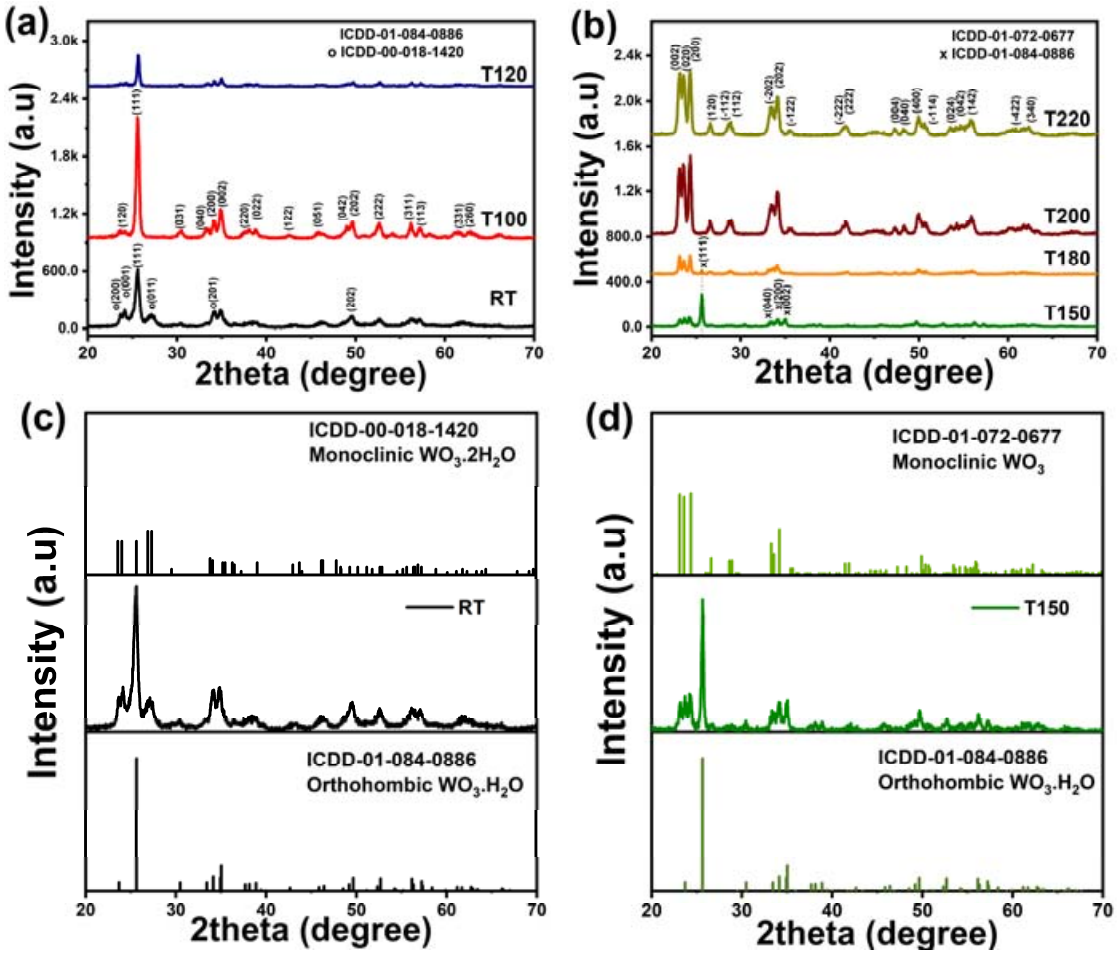

Fig. 2. (a-b) XRD patterns of the temperature-mediated samples, (c) XRD pattern of RT compared with standard pattern ICDD-01-084-0886 and ICDD-00-018-1420, and (d) XRD pattern of RT compared with standard pattern ICDD-01-084-0886 and ICDD-01-072-0677.

The XRD patterns of all samples are shown in Figs. 2a and 2b, which exhibit the variation of crystal properties of samples with reaction temperature. XRD analysis using HighScore plus software indicated that there were two phases of tungsten oxide in RT sample, i.e., monoclinic $WO_3 \cdot 2H_2O$ (ICDD 00-018-1420, space group P2/m, a = 7.50 Å, b = 6.93 Å, c = 3.70 Å, $\alpha = \gamma = 90^\circ$ and $\beta = 90.5^\circ$) and orthorhombic $WO_3 \cdot H_2O$ (ICDD 01-084-0886, space group Pmnb, $a = 5.24$ Å, $b = 10.71$ Å, $c = 5.13$ Åand $\alpha = \beta = \gamma = 90^\circ$), as shown in Fig. 2c. As the reaction time increased to 100 and 120°C (samples T100 and T120), only orthorhombic $WO_3 \cdot H_2O$ was observed in the samples (Fig. 2a). When the reaction time increased further to 150°C, besides the appearance of orthorhombic $WO_3 \cdot H_2O$, the signal of monoclinic WO_3 (ICDD-01-072-0677,

space group P21/n, $a = 7.31$ Å, $b = 7.54$ Å, $c = 7.92$ Å, $\alpha = \gamma = 90^\circ$ and $\beta = 90.881^\circ$) was also recorded (Fig. 2d), which implied a phase transformation from the orthorhombic $WO_3{\cdot}H_2O$ to monoclinic WO_3 as reaction temperature increased from 120 to 150°C. The phase transformation was also observed in the XRD pattern of the sample prepared at 180°C (sample T180 – Fig. 2b) and only completed when the reaction temperature reached 200°C. In the XRD patterns of the sample prepared at 200°C and higher temperatures (samples T200 and T220), only a characteristic peak of monoclinic WO_3 was observed. In all samples' XRD patterns, no signal of impurity was observed, and the XRD intensity decreased in samples having phase transition (RT, T120, T150, and T180). Based on XRD results, it is evident that when the reaction temperature increased from RT to 220°C, the crystal phase tungsten oxide transformed from monoclinic $WO_3 \cdot 2H_2O$ to orthorhombic $WO_3{\cdot}H_2O$, then to monoclinic WO_3. The phase junction between orthorhombic and monoclinic could be obtained at reaction temperatures of 120, 150, and 180°C.

The single-phase monoclinic samples (T180, T200, and T220) were further evaluated by using Williamson – Hall method (Eq. (1)) [28, 29]:

$$\beta \times \cos(\theta)\frac{0.9\lambda}{d} + 2\varepsilon \times \sin(\theta), \tag{1}$$

where β (rad) is the full width at half maximum of the peak at the diffraction angle 2θ (rad), λ (nm) is X-ray wavelength, ε (%) is the micro-strain, and d (nm) is the average crystalline size. The average crystalline size and micro-strain were inferred from the linear fit of data $\beta \times \cos(\theta)$ vs. $\sin(\theta)$. The extrapolated crystalline size and microstrain of monoclinic samples are presented in Table 1. It is noteworthy that when the reaction temperature increased from 180 to 200°C, the average crystalline size increased with the microstrain, which implied a higher crystallinity in sample T200 – in accord with the higher XRD signal. When the reaction temperature increased further to 220°C, the crystalline size and microstrain oppositely decreased, which was assigned to the breaking of WO_3 nanocuboid into smaller nanocuboid as observed in FESEM analysis.

Table 1. Extrapolated crystalline size and microstrain of monoclinic samples.

Sample	**T180**	**T200**	**T220**
Average crystalline size (nm)	35.6	44.9	33.4
Microstrain (%)	1.0	1.2	0.9

III.3. Raman analysis

Raman spectroscopy is a sensitive method for studying the crystallinity and the phase transformation of nanostructured materials. Fig. 3 presented Raman spectra of all samples, which implied the change of samples' phase with the reaction temperature. In sample RT's Raman spectrum, the characteristic peaks of both monoclinic $WO_3 \cdot 2H_2O$ and orthorhombic $WO_3{\cdot}H_2O$ were observed at 658, 945, and 956 cm^{-1} [30–32]. In Raman spectra of sample T100, only characteristic peak of orthorhombic $WO_3{\cdot}H_2O$ appeared, but in Raman spectra of samples T120, T150, and T180, the characteristic peaks of both orthorhombic $WO_3{\cdot}H_2O$ (at 638 and 945 cm^{-1}) and monoclinic WO_3 (at $\sim$ 711 and 806 cm^{-1}) were observed [16–18]. In samples prepared at higher

temperatures (T200 and T220), only characteristic peaks of monoclinic WO_3 were observed. Notably, that the Raman signal of monoclinic WO_3 increased relatively in comparison with the Raman signal of orthorhombic $WO_3 \cdot H_2O$ as reaction temperature increased (in samples T120, T150, and T180), and the Raman signal is higher in the sample prepared at higher reaction temperature (Fig. 3b). These results confirmed the phase transformation of samples with the reaction temperature, which is in accord with the XRD result.

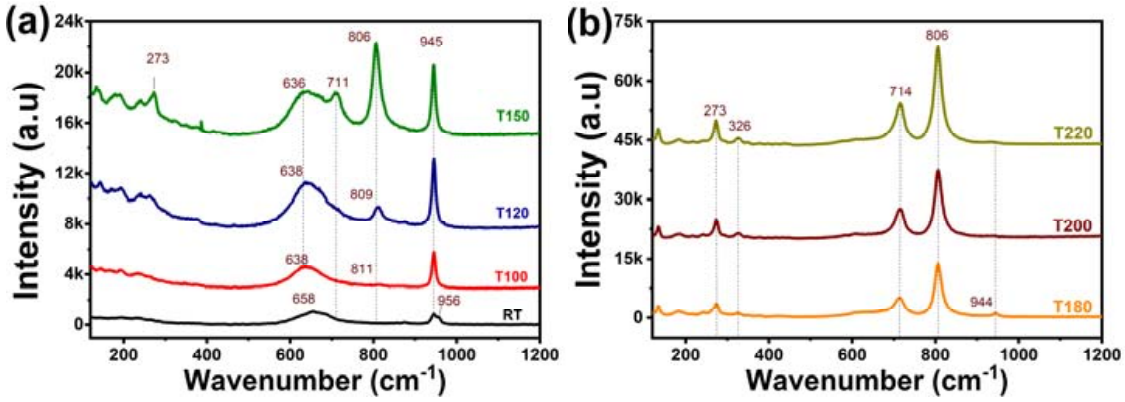

Fig. 3. Raman spectra of samples: (a) RT, T100, T120, and T150; (b) T180, T200, and T220.

III.4. Phase transformation mechanism

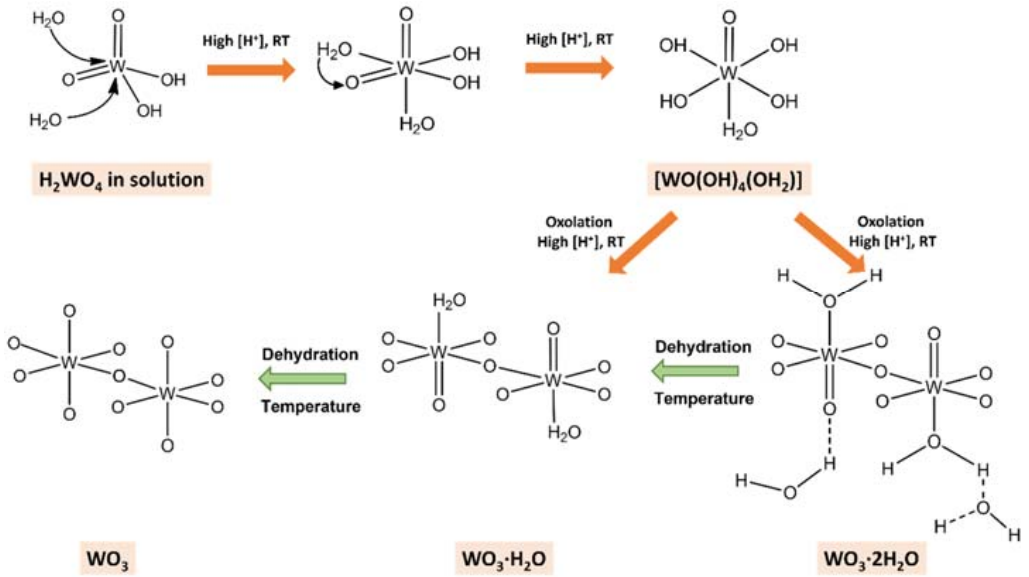

Scheme 1. Formation and transformation from $WO_3 \cdot 2H_2O$ to $WO_3 \cdot H_2O$ and WO_3 via oxolation and dehydration processes.

The transformation from monoclinic $WO_3 \cdot 2H_2O$ to orthorhombic $WO_3 \cdot H_2O$, then to monoclinic WO_3 could be explained by the oxolation and dehydration reactions during the hydrothermal process in a highly acidic environment (Scheme 1) [15,17–20]. In brief, tungstic acid (H_2WO_4) was initially formed via Eq. (2) by pouring HCl into Na_2WO_4 solution at the beginning of the precursor solution preparation [1, 21]:

$$Na_2WO_4 + 2HCl \longrightarrow 2NaCl^{+}H_2WO_4, \tag{2}$$

In a highly acidic environment, tungstic acid interacts with water molecules and transforms into the complex structure $[WO(OH)_4(OH_2)]$ like octahedra with four [-OH] groups in the equator plane (Eq. (3)) [10, 33]:

$$H_2WO_4 + 2H_2O \xrightarrow{\text{Solvent,Hight}[H^+]} [WO(OH)_4(OH_2)]. \tag{3}$$

These $[WO(OH)_4(OH_2)]$ complex structures will then aggregate via oxolation reaction to form monoclinic $WO_3 \cdot 2H_2O$ and orthorhombic $WO_3 \cdot H_2O$ structures even at RT (Eqs. (4) and (5)) [10, 33–35].

$$[WO(OH)_4(OH_2)] \xrightarrow{\text{Solvent, High}[H^+]} WO_3 \cdot 2H_2O + H_2O, \tag{4}$$

$$[WO(OH)_4(OH_2)] \xrightarrow{\text{Solvent, High}[H^+]} WO_3 \cdot H_2O + 2H_2O, \tag{5}$$

The oxolation reaction happens more strongly when the hydrothermal process starts, especially in a highly acidic environment. The high ion $[H^+]$ concentration platform in the highly acidic environment creates a high electric field environment, which then vigorously promotes the oxolation process at RT. When the reaction temperature increased, the dielectric constant of water decreased, resulting in the increase of the electric force [36, 37], which then pushed octahedra close together and triggered the dehydration process. The monoclinic $WO_3 \cdot 2H_2O$ was dehydrated to form orthorhombic $WO_3 \cdot H_2O$ (in samples T100 and T120) via Eq. (6), and the orthorhombic $WO_3 \cdot H_2O$ was driven to transform into the monoclinic WO_3 structure (in samples T150, T180, T200, and T220) during the hydrothermal process (Eq. (7)).

$$WO_3 \cdot 2H_2O \xrightarrow{\text{dehydration}} WO_3 \cdot H_2O + H_2O, \tag{6}$$

$$WO_3 \cdot H_2O \xrightarrow{\text{dehydration}} WO_3 + H_2O, \tag{7}$$

Note that, the oxolation process occurring on the equator plane results in crystal growth through the preferential shape of the plate with a preferential growth direction (010) in monoclinic $WO_3 \cdot 2H_2O$ and orthorhombic $WO_3 \cdot H_2O$. While during the dehydration process, in the homogeneous $[H^+]$ ion platform, the electric force tends to support the growth equally in the [200], [020], and [002] directions and results in the nanocuboid morphology [20,38]. In sample T150, the phase transformed from orthorhombic $WO_3 \cdot H_2O$ to monoclinic WO_3, so both nanoplate and nanocuboid appeared in the sample. Due to the beginning of the formation of the monoclinic phase, the dimension of the monoclinic nanocuboid in sample T150 was smaller in comparison with the dimension of the nanocuboid prepared at higher reaction temperatures (samples T180, T200, and T220) (Fig. 1). When the reaction temperature increased from 150 to higher temperatures (180, 200, and 220°C), the dehydration also became stronger, which then promoted the growth of monoclinic WO_3 nanocuboid with larger dimensions. But when the reaction temperature reached 220°C, the

electric force was strong enough to restrain/inhibit the growth of nanocuboid which resulted in the smaller average dimension of nanocuboid and smaller microstrain. Moreover, when the reaction temperature increases, the saturated vapor pressure of water in the hydrothermal process increases which then caused a decrease in the products' size [39, 40]. It is notable that the effect of the saturated vapor pressure on products' size becomes evident only when the phase transformation completes – at the high reaction temperatures (200 and 220˚C).

III.5. Optical properties

UV-Vis diffuse reflectance spectra of samples (Fig. 4) were used to evaluate the optical properties. The UV-Vis results showed that the absorption edge of all samples was in the visible-light region and was gradually blue-shifted towards shorter wavelengths as hydrothermal temperature increased. The blue shift of the absorption edge was assigned to the phase transformation of the sample with the increase in reaction temperature.

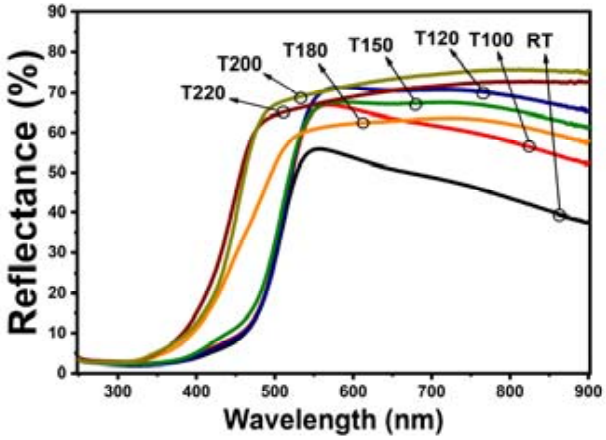

Fig. 4. Diffuse reflectance spectra of samples.

To evaluate the optical band gap of samples, the derivative of the Kubelka–Munk equation (Eq. 8) was used [29]:

$$\frac{d\{\ln F(R)\times h\nu\}}{d(h\nu)} = \frac{n}{h\nu - E}, \tag{8}$$

where $F(R)$ is the function of reflectance determined from diffuse reflectance R via the formula $F(R) = (1-R)^2/2R$, $h\nu$ is the energy of the incident photon, and $n = 1/2$ and 2 for direct and indirect allowed recombination, respectively [29]. The optical band gaps E_g of the samples were extracted from the plot of $d\{\ln[F(R)h\nu]\}/d(h\nu)$ versus $h\nu$ without depending on the value of n (Fig. 5). The results indicated the tendency of changing the optical band gap of the samples. In detail, samples RT, T100, T120, and T150 had an optical band gap of ~ 2.40 eV, sample T180 had an optical band gap of ~ 2.53 eV, while other samples (T200 and T220) had the optical band gap of 2.70 eV. Notably, all observed optical band gap values are in the visible range. The moderate optical band gap value of samples RT, T100, T120, and T150 (~ 2.40 eV) was assigned to the orthorhombic $WO_3{\cdot}H_2O$ structure which took the main part in these samples [41–44]. The

large optical band gap of ~ 2.70 eV of samples T200 and T220 was assigned to the monoclinic WO_3 which is similar to the values reported elsewhere [18, 45–47]. The abnormally optical band gap value (2.53 eV) of sample T180, which was in the middle between the values of orthorhombic $WO_3{\cdot}H_2O$ (2.40 eV) and monoclinic WO_3 (2.70 eV), was assigned to the strong phase transformation (the transition of DRS spectra – Fig. 4) from orthorhombic to monoclinic at this temperature. These results also conformed to the phase transformation observed in XRD and Raman analysis.

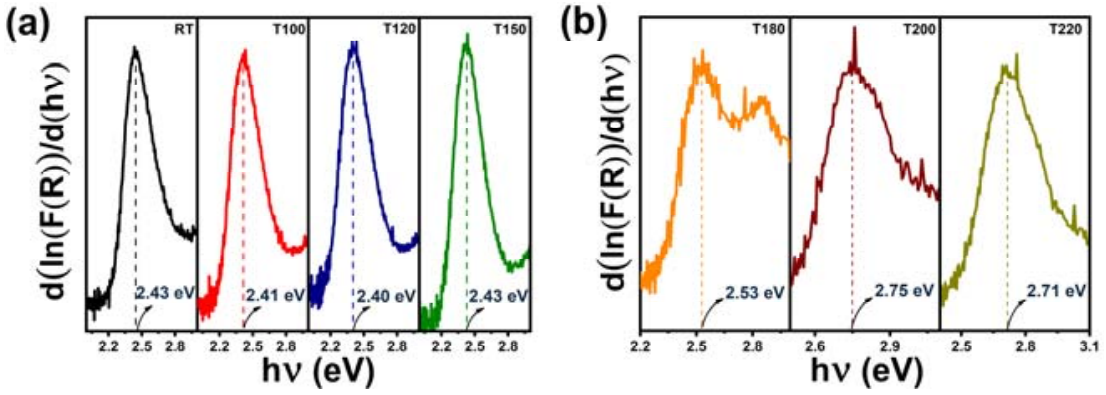

Fig. 5. Derivative plots of samples prepared at different reaction temperatures.

IV. CONCLUSION

Tungsten oxide nanostructures with different crystal phases were synthesized via a facile hydrothermal method at different reaction temperatures without using any structure-directing agent. The phase transformation of samples, followed by the change of morphology and optical band gap, was observed as the reaction temperature increased from RT (23˚C) to 220˚C. In detail, the crystal phase transformed from monoclinic $WO_3 \cdot 2H_2O$ to orthorhombic $WO_3{\cdot}H_2O$, then to monoclinic WO_3 as the reaction temperature increased from RT to 100˚C, then to 220˚C, respectively. Corresponding to the phase transformation, the optical band gap increased from 2.43 to 2.71 eV, and the morphology varied from nanoplate to nanocuboid. The phase transformation was assigned to the oxolation and dehydration processes, which occurred in a high $[H^+]$ concentration environment during the hydrothermal reaction. These results gave an insight into the phase transformation and implied a simple method for manipulating the crystal phase and morphology of tungsten oxide nanostructures for various applications.

ACKNOWLEDGMENT

This research is funded by Vietnam National Foundation for Science and Technology Development (NAFOSTED) under grant number 103.02-2020.39.

REFERENCES

[1] D. Bonardo, N. L. W. Septiani, F. Amri, Estananto, S. Humaidi, Suyatman et al., *Review—recent development of WO_3 for toxic gas sensors applications*, *J. Electrochem. Soc.* **168** (2021) 107502.

[2] G. Mineo, K. Moulaee, G. Neri, S. Mirabella and E. Bruno, *H_2 detection mechanism in chemoresistive sensor based on low-cost synthesized WO_3 nanorods*, *Sens. Actuators B Chem.* **348** (2021) 130704.
[3] S. Zeb, G. Sun, Y. Nie, H. Xu, Y. Cui and X. Jiang, *Advanced developments in nonstoichiometric tungsten oxides for electrochromic applications*, *Mater. Adv.* **2** (2021) 6839.
[4] J. Qiu, F. Xu, B. Jin, Y. Sun and J. Wang, *Hierarchical WO_3 microflowers with tailored oxygen vacancies for boosting photocatalytic dye degradation*, *New J. Chem.* **45** (2021) 21074.
[5] M. G. Peleyeju and E. L. Viljoen, *Wo_3-based catalysts for photocatalytic and photoelectrocatalytic removal of organic pollutants from water – a review*, *J. Water Process Eng.* **40** (2021) 101930.
[6] K. Thummavichai, Y. Xia and Y. Zhu, *Recent progress in chromogenic research of tungsten oxides towards energy-related applications*, *Prog. Mater. Sci.* **88** (2017) 281.
[7] P. A. Shinde and S. C. Jun, *Review on recent progress in the development of tungsten oxide based electrodes for electrochemical energy storage*, *ChemSusChem* **13** (2020) 11 [`https://chemistry-europe.onlinelibrary.wiley.com/doi/pdf/10.1002/cssc.201902071`].
[8] S. Cong, Z. Wang, W. Gong, Z. Chen, W. Lu, J. R. Lombardi et al., *Electrochromic semiconductors as colorimetric sers substrates with high reproducibility and renewability*, *Nat. Commun.* **10** (2019) 1.
[9] M. Jamali and F. S. Tehrani, *Thermally stable WO_3 nanostructure synthesized by hydrothermal method without using surfactant*, *Mater. Sci. Eng. B* **270** (2021) 115221.
[10] N. L. Pham, T. L. A. Luu, H. L. Nguyen and C. T. Nguyen, *Effects of acidity on the formation and adsorption activity of tungsten oxide nanostructures prepared via the acid precipitation method*, *Mater. Chem. Phys.* **272** (2021) 125014.
[11] M. Jamali and F. S. Tehrani, *Effect of synthesis route on the structural and morphological properties of WO_3 nanostructures*, *Mater. Sci. Semicond. Process.* **107** (2020) 104829.
[12] G. Adilakshmi, A. S. Reddy, P. S. Reddy and C. S. Reddy, *Electron beam evaporated nanostructure WO_3 films for gas sensor application*, *Mater. Sci Engineering: B* **273** (2021) 115421.
[13] F. Andrei, A. Andrei, R. Birjega, E. N. Sirjita, A. I. Radu, M. Dinescu et al., *The influence of the structural and morphological properties of WO_3 thin films obtained by pld on the photoelectrochemical water-splitting reaction efficiency*, *Nanomaterials* **11** (2021) 110.
[14] K. Ghosh, A. Roy, S. Tripathi, S. Ghule, A. K. Singh and N. Ravishankar, *Insights into nucleation, growth and phase selection of wo 3: morphology control and electrochromic properties*, *J. Mater. Chem. C* **5** (2017) 7307.
[15] L. T. L. Anh, P. T. Phong, H. V. Phuong, D. V. Truong, L. X. Truong, P. T. Son et al., *Tailoring the structure and morphology of WO_3 nanostructures by hydrothermal method*, *Vietnam J. Sci. Technol.* **56** (2018) 127.
[16] H. Xu, J. Gao, M. Li, Y. Zhao, M. Zhang, T. Zhao et al., *Mesoporous WO_3 nanofibers with crystalline framework for high-performance acetone sensing*, *Front. Chem.* **7** (2019) 266.
[17] A. V. Nikam, B. L. V. Prasad and A. A. Kulkarni, *Wet chemical synthesis of metal oxide nanoparticles: a review*, *CrystEngComm* **20** (2018) 5091.
[18] S. Adhikari and D. Sarkar, *Hydrothermal synthesis and electrochromism of wo 3 nanocuboids*, *RSC Adv.* **4** (2014) 20145.
[19] L. Wang, M. Huang, Z. Chen, Z. Yang, M. Qiu, K. Wang et al., *ph-controlled assembly of three-dimensional tungsten oxide hierarchical nanostructures for catalytic oxidation of cyclohexene to adipic acid*, *CrystEngComm* **18** (2016) 8688.
[20] C. T. Nguyen, N. L. Pham, T. T. Nguyen, D. T. Do and T. L. A. Luu, *Effect of reaction time on the phase transformation and photocatalytic activity under solar irradiation of tungsten oxide nanocuboids prepared via facile hydrothermal method*, *Phase Transitions* **94** (2021) 651.
[21] F. S. Tehrani, H. Ahmadian and M. Aliannezhadi, *Hydrothermal synthesis and characterization of WO_3 nanostructures: Effect of reaction time*, *Mater. Res. Express* **7** (2020) 015911.
[22] H. Zhang, Z. Liu, J. Yang, W. Guo, L. Zhu and W. Zheng, *Temperature and acidity effects on WO_3 nanostructures and gas-sensing properties of WO_3 nanoplates*, *Mater. Res. Bull.* **57** (2014) 260.
[23] Y. S. Liu, X. L. Xi, Z. R. Nie, L. Y. Zhao and Y. S. Fan, *Effect of hydrothermal conditions on crystal structure, morphology and visible-light driven photocatalysis of WO_3 nanostructures*, *Mater. Sci. Forum* **993** (2020) 893.
[24] T. Nagyné-Kovács, I. E. Lukács, A. Szabó, K. Hernadi, T. Igricz, K. László et al., *Effect of ph in the hydrothermal preparation of monoclinic tungsten oxide*, *J. Solid State Chem.* **281** (2020) 121044.

[25] K. Yang, X. Li, C. Yu, D. Zeng, F. Chen, K. Zhang et al., *Review on heterophase/homophase junctions for efficient photocatalysis: The case of phase transition construction*, *Chinese J. Catal.* **40** (2019) 796.
[26] M. Kang, J. Liang, F. Wang, X. Chen, Y. Lu and J. Zhang, *Structural design of hexagonal/monoclinic WO_3 phase junction for photocatalytic degradation*, *Materials Research Bulletin* **121** (2020) 110614.
[27] X. D. Liu, Q. Yang, L. Yuan, D. Qi, X. Wei, X. Zhou et al., *Oxygen vacancy-rich WO_3 heterophase structure: A trade-off between surface-limited pseudocapacitance and intercalation-limited behaviour*, *Chem. Eng. J.* **425** (2021) 131431.
[28] G. Williamson and W. Hall, *X-ray line broadening from filed aluminium and wolfram*, *Acta Metall.* **1** (1953) 22.
[29] C. T. Nguyen, T. P. Pham, T. L. A. Luu, X. S. Nguyen, T. T. Nguyen, H. L. Nguyen et al., *Constraint effect caused by graphene on in situ grown Gr@WO_3-nanobrick hybrid material*, *Ceram. Int.* **46** (2020) 8711.
[30] M. Daniel, B. Desbat, J. Lassegues, B. Gerand and M. Figlarz, *Infrared and raman study of WO_3 tungsten trioxides and WO_3, xH_2O tungsten trioxide tydrates*, *J. Solid State Chem.* **67** (1987) 235.
[31] H. S. Nguyen, T. L. A. Luu, H. T. Bui, T. T. Nguyen, H. L. Nguyen and C. T. Nguyen, *Facile synthesis of in situ cnt/$WO_3{\cdot}H_2O$ nanoplate composites for adsorption and photocatalytic applications under visible light irradiation*, *Semicond. Sci. Technol.* **36** (2021) 095010.
[32] V. T. Nguyen, H. S. Nguyen, V. T. Pham, T. T. M. Nguyen, T. L. A. Luu, H. L. Nguyen et al., *Tungsten oxide nanoplates: facile synthesis, controllable oxygen deficiency and photocatalytic activity*, *Commun. Phys.* **30** (2020) 319.
[33] M. Henry, J. P. Jolivet and J. Livage, *Aqueous chemistry of metal cations: hydrolysis, condensation and complexation*, *Chemistry, Spectroscopy and Applications of Sol-Gel Glasses* (1992) 153.
[34] L. Liang, J. Zhang, Y. Zhou, J. Xie, X. Zhang, M. Guan et al., *High-performance flexible electrochromic device based on facile semiconductor-to-metal transition realized by $WO_3{\cdot}\ 2H_2O$ ultrathin nanosheets*, *Sci. Rep.* **3** (2013) 1.
[35] S. Wu, Y. Li, X. Chen, J. Liu, J. Gao and G. Li, *Fabrication of $WO_3{\cdot}\ 2H_2O$ nanoplatelet powder by breakdown anodization*, *Electrochem. Commun.* **104** (2019) 106479.
[36] G. Akerlof and H. Oshry, *The dielectric constant of water at high temperatures and in equilibrium with its vapor*, *J. Am. Chem. Soc.* **72** (1950) 2844.
[37] B. B. Owen, R. C. Miller, C. E. Milner and H. L. Cogan, *The dielectric constant of water as a function of temperature and pressure1, 2*, *J. Phys. Chem.* **65** (1961) 2065.
[38] S. Adhikari, K. S. Chandra, D.-H. Kim, G. Madras and D. Sarkar, *Understanding the morphological effects of WO_3 photocatalysts for the degradation of organic pollutants*, *Adv. Powder Technol.* **29** (2018) 1591.
[39] G. W. Thomson, *The antoine equation for vapor-pressure data.*, *Chem. Rev.* **38** (1946) 1.
[40] Y. Fan, X. Xi, Y. Liu, Z. Nie, Q. Zhang and L. Zhao, *Growth mechanism of immobilized WO_3 nanostructures in different solvents and their visible-light photocatalytic performance*, *J. Phys. Chem. Solids* **140** (2020) 109380.
[41] N. H. Son, N. G. Nam, N. T. Anh, T. N. Bach, L. T. L. Anh, N. T. Tung et al., *Functionalization-mediated preparation via acid precipitation and photocatalytic activity of in situ Ag_2WO_4@ WO_3. H_2O nanoplates*, *ECS J. Solid State Sci. Technol.* **10** (2021) 054009.
[42] J. Ke, H. Zhou, J. Liu, X. Duan, H. Zhang, S. Liu et al., *Crystal transformation of 2d tungstic acid h2wo4 to WO_3 for enhanced photocatalytic water oxidation*, *J. Colloid Interface Sci.* **514** (2018) 576.
[43] K. Nishiyama, J. Sasano, S. Yokoyama and M. Izaki, *Electrochemical preparation of tungsten oxide hydrate films with controlled bandgap energy*, *Thin Solid Films* **625** (2017) 29.
[44] Y. Yang, J. Chen, X. Liu, M. Qiu, L. Liu and F. Gao, *Oxygen vacancy-mediated wo 3 nanosheets by etched $\{200\}$ facets and the efficient visible-light photocatalytic oxygen evolution*, *New J. Chem.* **43** (2019) 16391.
[45] W. Zhu, F. Sun, R. Goei and Y. Zhou, *Facile fabrication of rgo-WO_3 composites for effective visible light photocatalytic degradation of sulfamethoxazole*, *Appl. Catal. B Environ.* **207** (2017) 93.
[46] J. Zhou, S. Lin, Y. Chen, and A. M. Gaskov.
[47] P. P. González-Borrero, F. Sato, A. N. Medina, M. L. Baesso, A. C. Bento, G. Baldissera et al., *Optical band-gap determination of nanostructured WO_3 film*, *Applied Physics Letters* **96** (2010) 061909 [https://doi.org/10.1063/1.3313945].